# Heat Transfer to Sub- and Supercritical Water Flowing Upward in a Vertical Tube at Low Mass Fluxes: Numerical Analysis and Experimental Validation

Samuel O. Odu,[†] Pelle Koster,[†] Aloijsius G. J. van der Ham,*,[†] Martin A. van der Hoef,[‡] and Sascha R. A. Kersten[†]

[†]Sustainable Process Technology and [‡]Physics of Fluid Group, Faculty of Science and Technology, University of Twente, 7500 AE Enschede, The Netherlands

ⓢ *Supporting Information*

ABSTRACT: Heat transfer to supercritical water (SCW) flowing upward in a vertical heated tube at low mass fluxes ($G \leq 20$ kg/m^2 s) has been numerically investigated in COMSOL Multiphysics and validated with experimental data. The turbulence models, essential to describing local turbulence, in COMSOL have been checked under conditions in which empirical heat-transfer correlations are available, and it is concluded that the shear-stress transport (SST) turbulence model gives the most accurate results. The numerical results obtained show a buoyancy induced circulation of the fluid resulting from

gravitational force acting on density gradients as well as a thin thermal boundary layer with a steep temperature gradient at the inner wall and a flat temperature profile in the bulk fluid. The heat-transfer coefficient of SCW is enhanced near the pseudo-critical temperature (T_{pc}) and is deteriorated at temperatures above T_{pc}. A new heat-transfer correlation has been developed and validated with experimental data.
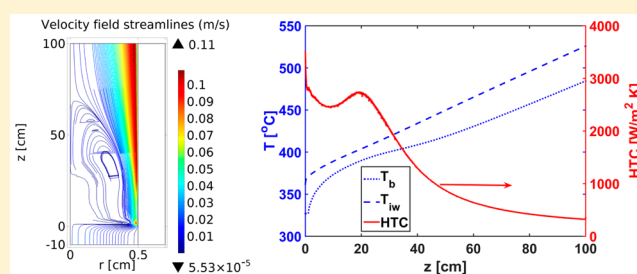
1. INTRODUCTION

Supercritical water (SCW) has found many applications in the last decades and the range of applications keep growing with time. Several applications are based on SCW being a "green" solvent, its properties being tunable by changes in temperature and pressure, and its solvation behavior for a variety of substances.[1] SCW has been used as a reaction medium for the conversion of biomass to hydrogen and natural gas[2,3] and liquid fuels[4] for the total oxidation of hazardous materials (supercritical water oxidation, SCWO)[5−8] as well as organic synthesis. SCW has been proposed as a coolant for nuclear reactors, allowing for high heat transfer and increased thermal efficiency.[9] SCW also has potential in desalination for the production of drinking water with zero liquid discharge.[10]

Supercritical water processes are energy intensive (about 2 GJ of energy is required to bring 1 m^3 of water from atmospheric conditions ($P = 1.02$ bar and $T = 25$ °C) to supercritical conditions ($P_c = 221$ bar and $T_c = 375$ °C). To make supercritical water processes a commercial success, heat integration is required to regain as much energy as possible from the process. To achieve this, the feed stream is heated by the supercritical product stream in a heat exchanger that operates at sub- to supercritical water conditions. In this heat exchanger, the feed will turn supercritical and the product stream will become liquid (subcritical), resulting in significant changes in properties such as the density, viscosity, heat capacity, and thermal

conductivity (see Figure S1), which significantly influence the heat-transfer characteristics.[11]

Currently, most research on SCW heat transfer is focused on using SCW as a coolant in large-scale nuclear reactors, which requires high mass fluxes ($G > 200$ kg/m^2.s).[9,12−15] However, for designing pilot-plant-scale SCW processes, such as supercritical desalination[10] and supercritical water gasification,[3] it may be required to know the heat-transfer characteristics of SCW at low mass fluxes (typically $G \leq 20$ kg/m^2.s). At these low mass fluxes (mostly laminar flows, Re < 2300), heat transfer may be either deteriorated or enhanced due to natural convective forces, which do not play an important role at high mass fluxes (turbulent flows).[15]

To the best of our knowledge, the work of Withag et al.[16] is the only work on heat transfer to SCW at low mass fluxes reported in the literature. Withag et al.[16] performed experiments and carried out 2D numerical simulations on supercritical water flowing upward in a vertical tube with mass fluxes ranging from 6.6 to 10.0 kg/m^2 s in COMSOL Multiphysics using the low Reynolds $k−\varepsilon$ model. Although the numerical simulation correctly predicted the shape of the temperature

profile measured in their experimental apparatus, the experimental values were overpredicted.

In general, essential insights into the heat-transfer characteristics as well as an engineering correlation for heat transfer in supercritical water at these low mass fluxes necessary for designing heat-transfer equipment, especially for pilot scale supercritical water processes, are lacking. The objective of this work is to provide these insights by numerical simulation and experimental validation. First, a 2D model is set up in a commercial CFD package, COMSOL Multiphysics 5.0 (which we hereafter denote as COMSOL), and calculations are performed to check if the model can accurately describe temperature profiles and heat transfer for flow conditions with known Nusselt correlations (see the Supporting Information). Next, 2D simulations are performed for the up-flow of water in a heated vertical tube under sub- and supercritical conditions to calculate the flow patterns and temperature profiles as well as heat-transfer coefficients. The influence of mass flux and tube diameter on heat-transfer characteristics is investigated. The results of the 2D model for the up-flow in a heated tube are validated with experiments in a newly designed apparatus. Finally, a 1D Nusselt correlation for engineering design is proposed and validated with experimental results.

2. THEORETICAL BASIS

2.1. Governing Equations. The equations that describe a steady, compressible two-dimensional flow follow from the laws of conservation of mass, momentum, and energy.[17,18] The mass and momentum equations, eqs 1 and 2, respectively, represent the steady-state compressible Reynolds averaged Navier–Stokes (RANS) equations for turbulent flows

$$\nabla\cdot(\rho\mathbf{u}) = 0 \tag{1}$$

$$\rho(\mathbf{u}\cdot\nabla)\mathbf{u} = \nabla\cdot(-p\mathbf{I}) + \nabla\cdot\left[(\mu + \mu_T)(\nabla\mathbf{u} + (\nabla\mathbf{u})^T)\right.$$
$$\left. - \frac{2}{3}(\mu + \mu_T)(\nabla\cdot\mathbf{u})\mathbf{I}\right] - \nabla\cdot\left(\frac{2}{3}\rho k\mathbf{I}\right) + \mathbf{F} \tag{2}$$

The volume force vector, $\mathbf{F}$, accounts for the gravity force that act downward in the z-direction.

$$\mathbf{F} = \begin{bmatrix} \mathbf{F}_r \\ \mathbf{F}_z \end{bmatrix} = \begin{bmatrix} 0 \\ -\rho g \end{bmatrix} \tag{3}$$

The conservation of energy is described by

$$\rho C_p \mathbf{u}\cdot\nabla T = \nabla\cdot(\lambda_{\mathrm{eff}}\nabla T) \tag{4}$$

where λ_{eff} is the effective thermal conductivity.

2.2. Turbulence Modeling. Although the radial-averaged Reynolds number for the low-flux SCW heat-transfer model is expected to be below 2300 (i.e., laminar flow), some local turbulence is expected due to the increased flow near the wall caused by natural convection induced by the gravity force acting on the significant change in density (see Figure S1) around the pseudocritical temperature (temperature at the maximum C_p; see Figure S1). Metais and Eckert[19] have shown that transition to turbulence may occur at Reynolds numbers as low as 200 for natural convection induced flows. It is therefore necessary to include an accurate turbulence model in the COMSOL simulations.

To determine which turbulence model will best represent our system, preliminary simulations were carried out in COMSOL in three flow regimes for which correlations are available in the literature: laminar and turbulent flows under normal temperature and pressure conditions, and turbulent supercritical water flow (see Figures S3, S4, and S5 for the results). The shear-stress transport (SST) turbulence model was found to give the most accurate results in these flow regimes and was therefore chosen as the turbulence model for further simulations.

The SST model combines the robustness of the $k-\varepsilon$ turbulence model in the bulk of the fluid and the $k-\omega$ turbulence model in the near-wall region. In addition, the SST model utilizes a y^+-insensitive (where y^+ is the near-wall grid resolution) wall treatment, which has been found to improve its predictive accuracy for general industrial applications while eliminating the user influence in grid generation.[20] Accurate solutions require $y^+ < 1$.[21] For more information on the SST model, see the work of Versteeg and Malalasekera,[18] Menter et al.,[20] and the COMSOL CFD user guide.[21]

The heat flux in eq 4 is modeled using the Kays–Crawford heat turbulence model.[22] The turbulence model takes into account the contribution of turbulent fluctuations to the temperature field. See Kays et al.[22] for detailed explanation of the Kays–Crawford heat turbulence model.

2.3. Natural Convection. Natural convection or free convective flow is induced by buoyancy forces. When temperature differences are introduced through boundaries maintained at different temperatures, the resulting density differences will induce motion; hot fluid tends to rise, and cold fluid tends to fall.[23] When both forced and natural convection are present in a system, this is called mixed convection.[15] There are two types of mixed convection: (i) aiding flow, when natural convection acts in the same direction as forced convection; and (ii) opposing flow, where natural convection acts in the opposite direction to forced convection.[15] In this work, only aiding flow will be considered. This means that heated flows are always flowing upward. Natural convection is modeled with eq 3 as part of the RANS equation.

2.4. Properties of Water in the Critical and Supercritical Region. The thermophysical properties of water are estimated with industrial formulations of the IAPWS (International Association for the Properties of Water and Steam).[11,24,25] These formulations, based on experimental data, calculate the desired properties in the critical region with an error as given in Table 1. Thermophysical properties of water as functions of

Table 1. Error of the IAPWS Formulations with Experimental Data at 300 bar for 327 °C < T < 527 °C

property	error	source
C_p	3%	IF-97[11]
ρ	0.2%	IF-97[11]
μ	3%	IAPWS viscosity[25]
λ	2%	IAPWS thermal conductivity[24]

temperature and pressure are shown in Figure S1. The temperature at the maximum value of C_p is called the pseudocritical temperature, T_{pc}, and it is pressure-dependent. At 270 bar, $T_{pc} = 392$ °C, and at 300 bar, $T_{pc} = 402$ °C. The physical properties of the fluid are imported to the COMSOL model using the Matlab implementation of the IAPWS formulations called XSteam.[26]

2.5. Discretization and Boundary Conditions. A 2D-axis-symetrical geometry is constructed in COMSOL. Dimensions of the test sections are given in Table 2, and a schematic is

Table 2. Parameters for the 2D Heated-Tube Model

mass flux, G (kg/m^2.s)	3.0, 7.0, 20.0
pressure, P (bar)	300
inlet temperature, T_{in} (°C)	27, 127, 327
outer-wall temperature, T_{ow} (°C)	177−527, 377−527
tube diameter, d_t (cm)	1, 2, 4
inlet Reynolds number, Re_{in}	200−2000
tube Reynolds number, Re_t	200−9000
Grashof number, Gr	$3 \times 10^6 - 9 \times 10^{10}$
Prandtl number, Pr	0.67−3.6
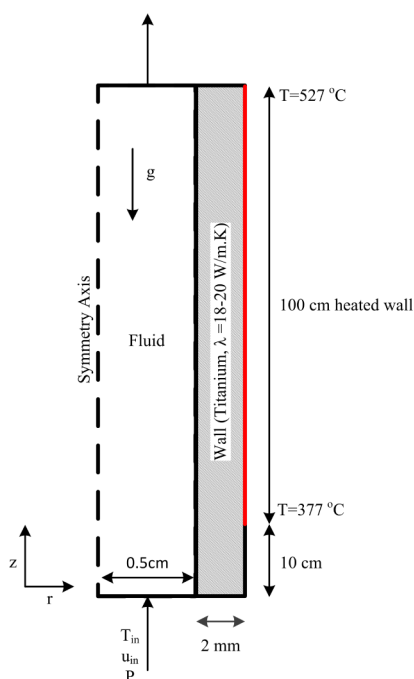
Figure 1. Geometry of the heated tube (base case) model.

shown in Figure 1. The water inlet is placed at the bottom of the tube. The inlet velocity is given as a parabolic laminar flow profile, and a uniform inlet temperature is set. An inlet region (10 cm, with z from −10 to 0 cm) is assigned to put some distance between the model boundary and the physics domain to improve model stability.[21] A linearly increasing temperature profile is specified at the outer walls (insulated from the environment) with the exception of the experimental validation simulations (section 5) where the outer wall temperature profiles obtained from the experiments are specified. The outlet is defined as a pressure boundary with the pressure specified. The tube inner wall has been modeled with the no-slip boundary condition for fluid flow.

The numerical grid is 2D-axis-symmetrical and consists of triangular elements. It is refined near the heated wall and expands toward the center of the tube. Near-wall cells are 0.008 mm in size and grow to 0.5 mm at the center of the tube (see Table S1 and Figure S2 for grid sensitivity analysis). A near-wall resolution y^+ value of 0.4 has been used in the simulations.

The heated tube model simulation with G_t = 7 kg/m^2 s, d_t = 1 cm, T_{in} = 327 °C, and T_{ow} = 377−527 °C will from hereon be referred to as the heated tube base case.
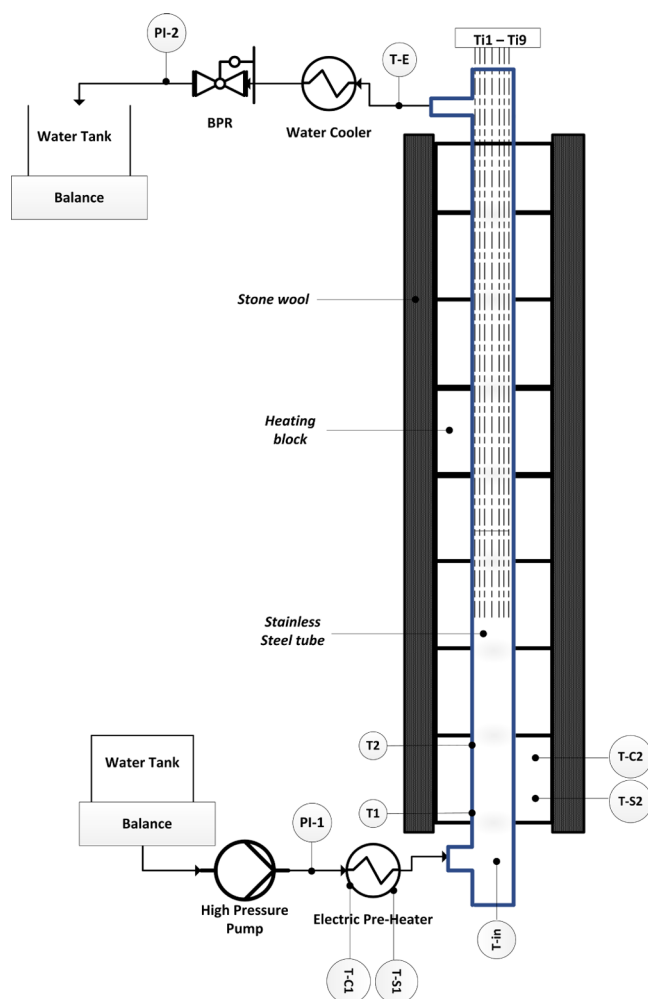

Figure 2. Schematics of the heated-tube experimental apparatus.

Table 3. Test Conditions for Validation of the 2D COMSOL mModel and Proposed 1D Nusselt Correlation

	case A	case B
$\dot{m}$ (kg/h)	4.1	8.0
G (kg/m^2.s)	3.2	6.2
P (bar)	300	300
T_{in} (°C)	104	86
T_{ow} (°C)	210−399	211−398

2.6. Post-Processing. The post-processing of the results consists mainly of averaging the 2D solutions, which are functions of the r- (radial) and z- (axial) directions to obtain 1D results, which are dependent only on the z-direction.

The average temperature of the fluid is determined by the mixing cup temperature and is calculated using eq 5.

$$T_{mc}(z) = \frac{\int_{R_i}^{R_o} 2\pi r \cdot G(r, z) \cdot C_p(r, z) \cdot T(r, z) \cdot \mathrm{d}r}{\int_{R_i}^{R_o} 2\pi r \cdot G(r, z) \cdot C_p(r, z) \cdot \mathrm{d}r} \tag{5}$$

The other temperature that is important is the temperature of the fluid at the inside wall T_{iw}. The 1D averaged fluid properties are evaluated at the operating pressure and $T = T_{mc}$, resulting in ρ_{mc}, $C_{p,mc}$, etc. because they are a strong function of temperature around the critical point.

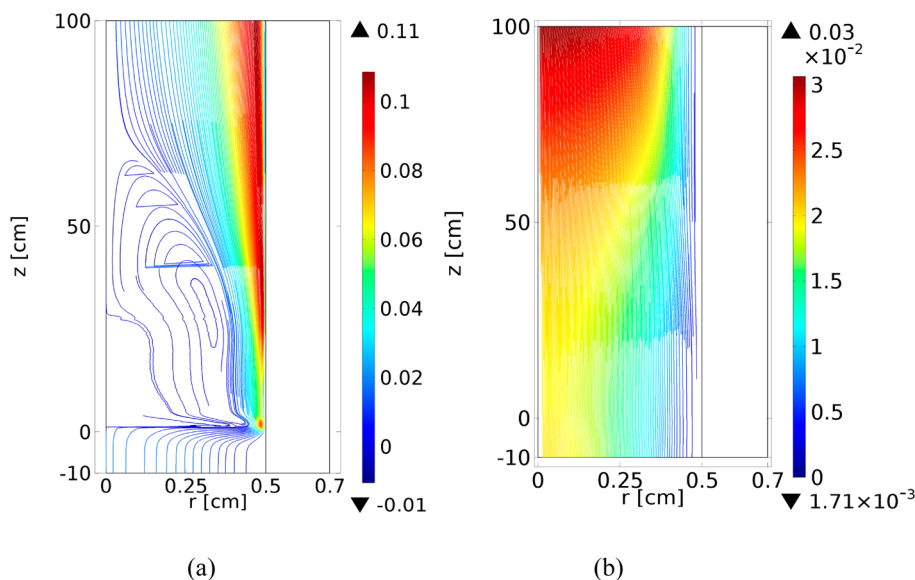(a)   (b)

Figure 3. Velocity streamlines (m/s) of the heated tube base case (a) and the base case without volume force (eq 3) in the RANS equation (b): fluid is $r = 0-0.5$ cm, and the wall is $r = 0.5-0.7$ cm.

The following dimensionless numbers are defined:

$$\text{Nu} = \frac{h \cdot d_t}{\lambda} = \frac{\phi''_{h,w} \cdot d_t}{(T_{iw} - T_{mc}) \cdot \lambda_{mc}} \tag{6}$$

$$\text{Re} = \frac{G \cdot d_t}{\mu_{mc}} \tag{7}$$

$$\text{Pr} = \frac{C_{p,mc} \cdot \mu_{mc}}{\lambda_{mc}} \tag{8}$$

$$\text{Gr} = \frac{g \cdot \beta_{mc} \cdot (T_{iw} - T_{mc}) \cdot d_t^3 \cdot \rho_{mc}^2}{\mu_{mc}^2} \tag{9}$$

3. EXPERIMENTAL SECTION

To validate the results of the 2D COMSOL simulations as well as the proposed 1D Nusselt correlation, an experimental apparatus has been designed and constructed. Temperature measurements at different radial and axial positions in water flowing at sub- and supercritical conditions has been obtained. A detailed description of the apparatus as well as validation results is provided in this section.

3.1. Experimental Apparatus. The schematics of the experimental apparatus is shown in Figure 2. The main part of the apparatus consists of a stainless steel tube (with an inner diameter of 2.14 cm, an outer diameter of 3.41 cm, and a length of 154 cm) fitted with eight aluminum heating blocks that keep the tube outer wall at a preset temperature. The heating blocks are insulated from the environment with stone wool to reduce heat losses.

Pressures up to 400 bar were provided to the tube with a high-pressure pump (LEWA diaphragm pump LDC1, LEWA Herbert Ott GmbH & Co KG, Germany, maximum P of 400 bar and maximum flow of 25.0 L/h) and controlled with a back-pressure regulator (TESCOM 26-1762-24A, Tescom Europe GmbH & Co. KG, Germany, $C_v = 0.14$). The uncertainty in pressure was 0.3% (0.9 at 300 bar), while the uncertainty in mass-flow measurement was 1%. The water is preheated by an
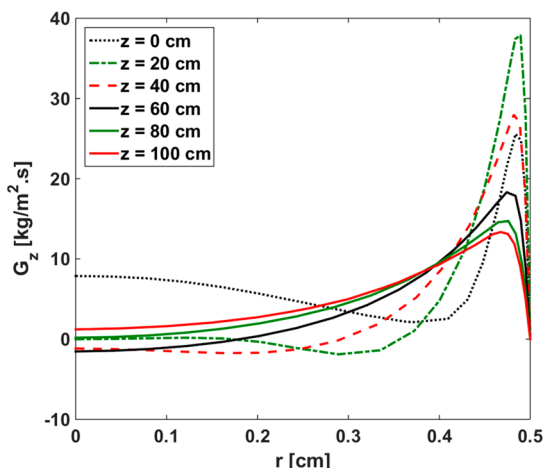

Figure 4. Variation of axial mass flux along the tube radius at different axial positions for the heated-tube base case.
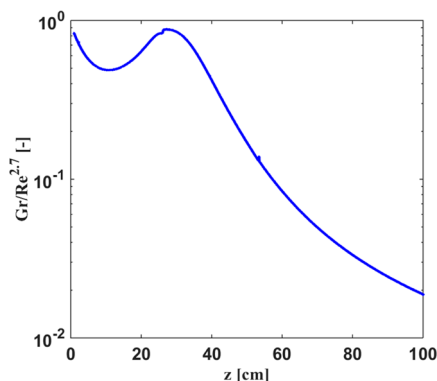

Figure 5. Variation of $\text{Gr}/\text{Re}^{2.7}$ along the tube length for the heated-tube base case.

electric heater (T-C1 is for temperature control, and T-S1 is for the set safety temperature) until the desired inlet temperature is attained. The water is heated as it flows upward in the tube with the aid of the aluminum heating blocks. Each heating block can
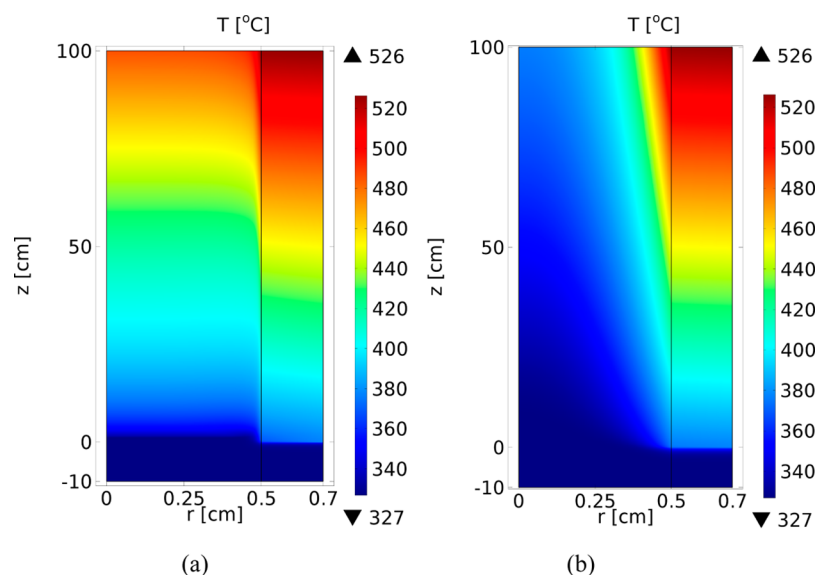
Figure 6. Temperature profile of the heated-tube base case (a) and the base case without volume force (eq 3) in the RANS equation (b). Fluid is $r = 0$–0.5 cm, and the wall is $r = 0.5$–0.7 cm.
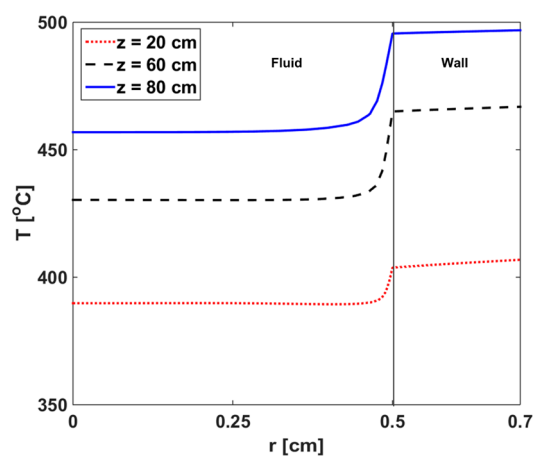

Figure 7. Radial temperature profiles at $z = 20$, 60, and 80 cm, respectively, for the heated-tube base case.

be set to a desired temperature (by adjusting T-C2), and the temperature at the tube outer wall in each heating block section is measured at the top and bottom parts of the section with T2 and T1, respectively. The experimental apparatus can be operated at pressures up to 350 bar and temperatures up to 500 °C.

A total of nine thermocouples (Ti1–Ti9), held at different predefined radial positions but at the same axial position by a movable thermocouple holder, measure the radial temperature profile in the tube at different heights. All temperatures were measured using standard type-K thermocouples (uncertainty in temperature measurement is 0.4% of measured value in °C, while the relative difference of measured values between thermocouples is 0.2 °C).

At the tube outlet, the water is cooled to a temperature below 70 °C (temperature limit of the back pressure regulator) with a shell and tube water cooler and then depressurized. Masses in and out are weighed to ensure mass balance closure. Temperatures (outer wall and inside the heated tube) are monitored and recorded (at the steady state) with the aid of the PicoLog data acquisition program.

3.2. Experimental Procedure and Test Conditions. At the start of each measurement, the thermocouple holder is moved to the desired axial position, and then the pump is switched on. The desired operating pressure in the tube is attained by adjusting the air-controlled back pressure regulator (BPR). A cold test is carried out to check for leakage. Next, the preheater is turned on and adjusted to obtain the desired inlet temperature. Thereafter, the heating blocks are switched on and set to the desired values. The outer wall temperatures as well as the temperature inside the tube are monitored with the aid of the PicoLog data acquisition program. When steady state is attained (fluctuations of not more than 1 °C in all measured temperatures over a period of 10 min), the data is recorded. At the end of data acquisition, the apparatus is depressurized and cooled. The thermocouple holder is then moved to the next measurement position (axial), and the procedure described above is repeated.

Measurements are carried out at tube axial positions 24, 44, 64, 84, 104, 124, and 144 cm, respectively. Test conditions are summarized in Table 3. The test cases are modeled in COMSOL with tube dimensions, mass flow, pressure, inlet temperature, and outer-wall temperature profiles (all obtained from experiments) as the model input parameters and with stainless steel chosen as the tube material.

4. RESULTS OF 2D COMSOL SIMULATIONS

4.1. Heated Tube Base Case Model. Results of the heated tube base case ($G = 7$ kg/m^2 s, $d_t = 1$ cm, $T_{in} = 327$ °C, and $T_{ow} = 377$–527 °C) are presented and discussed. The obtained velocity profile (streamlines) and the variation of the axial mass flux along the tube radius at different axial positions for the steady-state simulation are shown in Figures 3a and 4, respectively.

Figure 3a shows three regions: (i) a stagnant zone around the center of the tube (in the region $0 < r < 0.15$ cm and $0 < z < 30$ cm), (ii) an adjacent circulation zone, and (iii) a flow region with a growing momentum boundary layer at the near-wall region. At the beginning of the heat-transfer area ($z = 0$ cm), the incoming fluid comes in contact with the circulating and stagnant bulk and is (abruptly) transported to the wall. As the
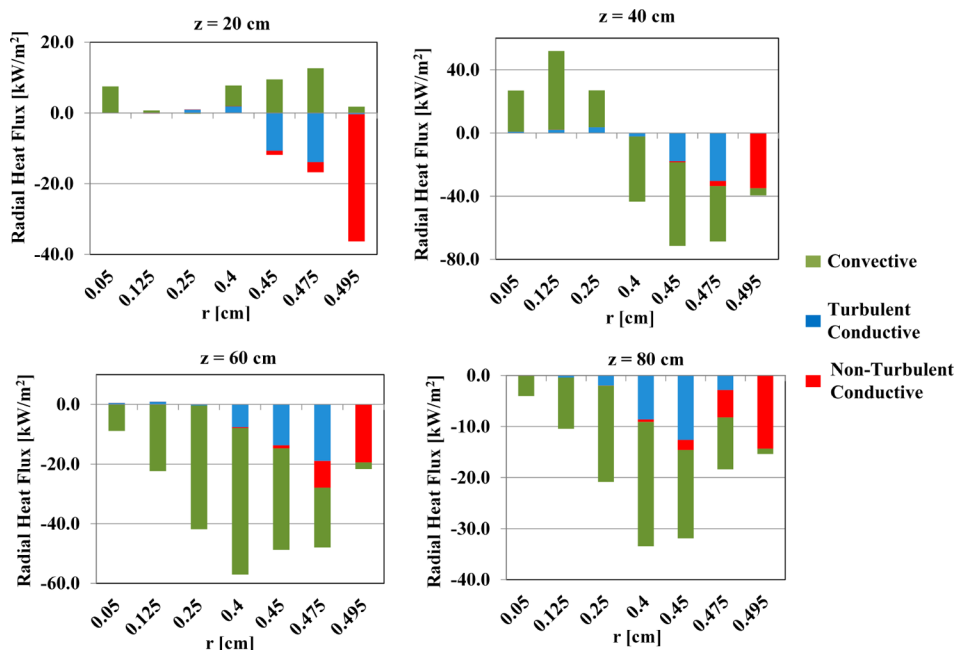
Figure 8. Radial heat flux variation over the radius at different axial positions for the heated-tube base case (see eqs 11–13 for definitions of the heat fluxes): positive values denote the direction is toward the wall, while negative values denote the direction is toward the center of the tube.

fluid comes into contact with the heated wall surface, a boundary layer is formed due to the actions of buoyancy forces, which drag the fluid along the wall leaving a mostly stagnant region in the bulk of the fluid.

Along the length of the heated tube, an increased upward velocity near the wall (about 10× the inlet velocity) is observed. This is a direct result of the fluid near the wall heating up and consequently significantly decreasing density compared to the bulk fluid. This results in a vertical force accelerating the fluid in the upward direction near the wall and thus decreasing the velocity in the bulk. Natural convection induced circulation flow from the wall into the bulk of the fluid and back creates mixing. This circulation flow is reflected in the negative axial mass fluxes at z = 20, 40, and 60 cm, as shown in Figure 4.

Figure 3b shows the velocity streamlines for the same simulation without the volume force (eq 3) as part of the RANS equation. The velocity profile obtained is that of a laminar flow without the influence of natural convection with the maximum velocity at the center of the tube, and the lowest velocity at near-wall region (see Figure 6b for the surface temperature plot). We can conclude that the flow pattern in Figure 3a is a buoyancy-induced motion resulting from the volume force (gravity force) acting on density gradients, which arise from temperature gradients in the fluid.

Jackson and Hall[27] have provided a general criterion (eq 10) for when the influences of buoyancy become negligible for supercritical fluids in vertical flows. Above the proposed limit, the higher the value for $Gr/Re^{2.7}$, the larger the influence of buoyancy.

$$\frac{Gr}{Re^{2.7}} < 10^{-5} \tag{10}$$

Figure 5 shows that the values of $Gr/Re^{2.7}$ obtained for the base case simulation are much higher than the proposed limit of Jackson and Hall,[27] indicating a dominant influence of buoyancy.
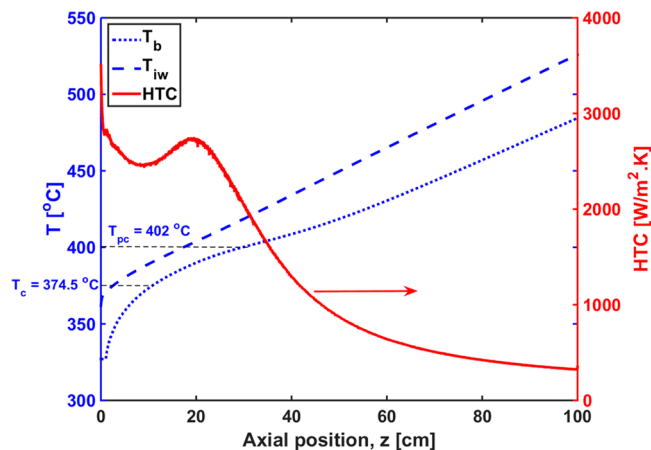

Figure 9. Bulk temperature, tube inner-wall temperature, and HTC profile as a function of axial position for heated-tube base case.

The surface plots of the temperature profile are shown in Figure 6a for the heated tube base case and Figure 6b without the volume force as part of the RANS equation. In Figure 6a, a flat temperature profile (absent in Figure 6b) is observed in the bulk, indicating that the buoyancy-induced circulation flow increases mixing in the fluid bulk. In addition, a thermal boundary layer of about 0.5 mm from the heated surface with a steep temperature gradient is observed. The radial temperature profile can be seen more clearly in Figure 7. The temperature from the outer tube wall to the tube center at three different axial position is plotted against the tube radial coordinates. A radial temperature gradient is observed only in the region 0.5 mm away from the tube inner wall. The temperature gradient in the thermal boundary layer as well as the thickness of the boundary layer is observed to increase as the fluid moves away from the circulation zone.

Heat transport in the fluid domain is by convection and conduction (turbulent and nonturbulent contributions). The non-turbulent conductive ($\phi_{h,cond}''$), turbulent conductive ($\phi_{h,T}''$), and
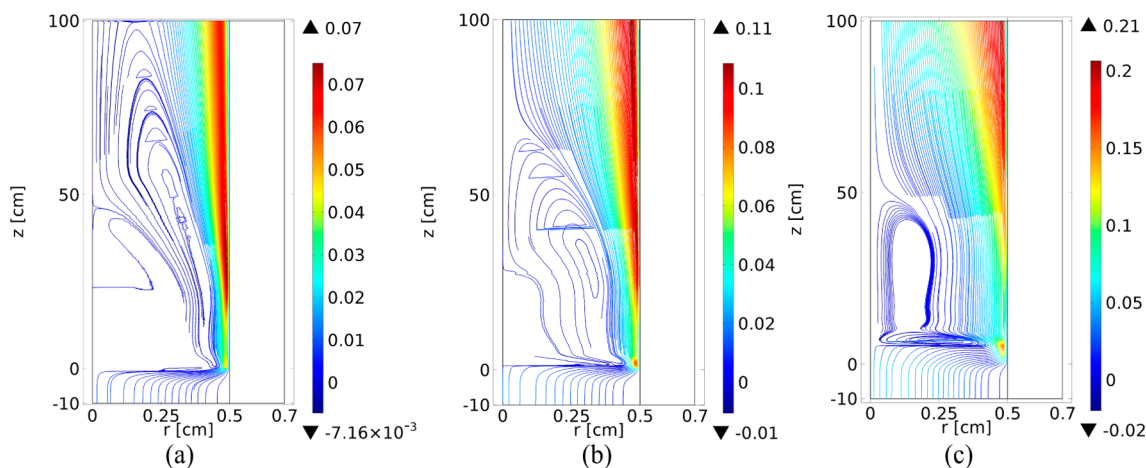
Figure 10. Velocity streamlines (m/s) for mass fluxes 3 (a), 7 (b), and 20 kg/m^2 s (c) for d_t = 1 cm, T_{in} = 327 °C, and T_{ow} = 377−527 °C; fluid is r = 0−0.5 cm, and the wall is r = 0.5−0.7 cm.

convective ($\phi''_{h,conv}$) heat fluxes are defined in eqs 11, 12, and 13, respectively. Figure 8 shows the variation of the contributions of the convective and conductive heat fluxes to the total radial heat flux along the radius at different axial positions. Positive values depict heat flux toward the wall, while negative values denote heat flux toward the tube center. While the fluid in the thermal boundary layer (0.45 < r < 0.5 cm) is heated by thermal conduction and convection in the radial direction, very close to the wall (r = 0.495 cm), heat is primarily transferred to the fluid by nonturbulent conduction. Away from the thermal boundary layer toward the center of the tube, radial heat transport is primarily due to convection.

$$\phi''_{h,cond} = -\lambda . \nabla T \tag{11}$$

$$\phi''_{h,T} = -\lambda_T \cdot \nabla T \tag{12}$$

$$\phi''_{h,conv} = \rho \cdot \mathbf{u} \cdot \left(H - \frac{P}{\rho} \right) \tag{13}$$

Figure 9 shows the heat-transfer coefficient (HTC), tube inner-wall temperature, and the tube center (bulk) temperature as a function of the axial position. The HTC is observed to go through a peak (2750 W/m^2·K) at T_{iw} = 402 °C and T_b = 389 °C and then decreases rapidly to about 300 W/m^2·K. This shows a deteriorated heat transfer in SCW laminar flow at temperatures above the pseudocritical temperature. Above the pseudocritical temperature, the properties of supercritical water becomes more gas-like under isobaric conditions. This might account for the deteriorated heat-transfer coefficient obtained at these temperatures.

4.2. Effect of Mass Flux. The effect of mass flux was investigated for 3, 7, and 20 kg/m^2·s in a tube diameter of 1 cm, inlet temperature of 327 °C, and linearly increasing wall temperature of 377−527 °C. The velocity streamlines are shown in Figure 10 (see Figure S6 for the axial mass flux plots). As the mass flux (and consequently mass flow, because tube diameter is constant) increases, the sizes of the circulation zone and stagnant zone decrease.

Figure 11 shows the values of Gr/Re$^{2.7}$ to be higher than the proposed limit of Jackson and Hall[27] (eq 10) for all mass fluxes investigated, indicating that buoyancy effects are present. However, the influence of buoyancy decreases with increasing mass flux.
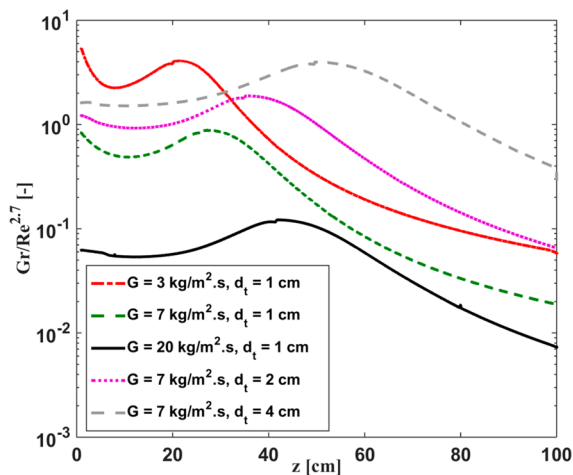

Figure 11. Variation of Gr/Re$^{2.7}$ along the tube length for the different mass fluxes and tube diameters.

As shown in the dimensionless radial temperature plot at tube axial positions 20 and 60 cm, respectively (Figure 12), there is no substantial influence of mass flux (in the range
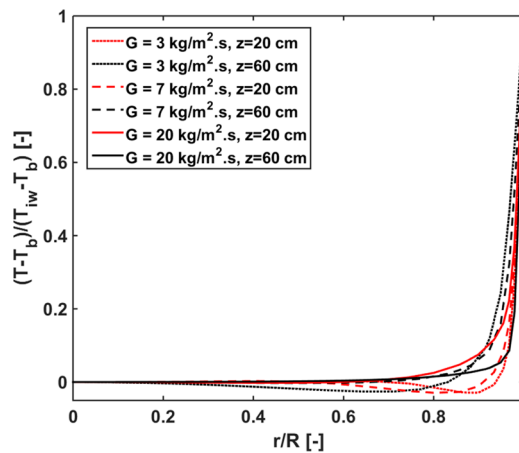

Figure 12. Dimensionless radial temperature profiles for the different mass fluxes at z = 20 and 60 cm, respectively, for d_t = 1 cm, T_{in} = 327 °C, and T_{ow} = 377−527 °C.
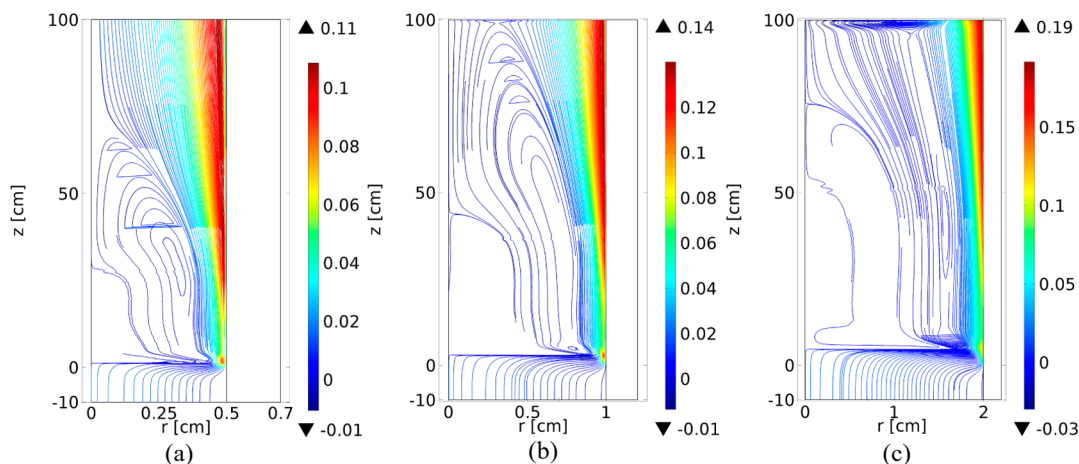
Figure 13. Velocity streamlines (m/s) for tube diameters 1 (a), 2 (b), and 4 cm (c) for G = 7 kg/m^2 s, T_{in} = 327 °C, and T_{ow} = 377−527 °C.
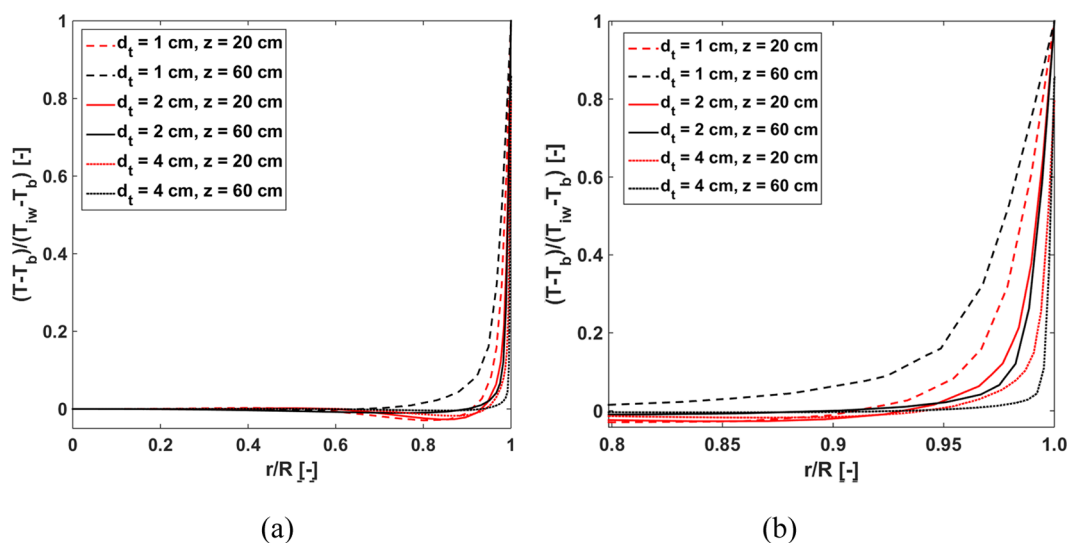

Figure 14. Dimensionless radial temperature profiles for the different tube diameters at z = 20 and 60 cm, respectively, for G = 7 kg/m^2 s, T_{in} = 327 °C, and T_{ow} = 377−527 °C (a) and with the near-wall region enlarged (b).
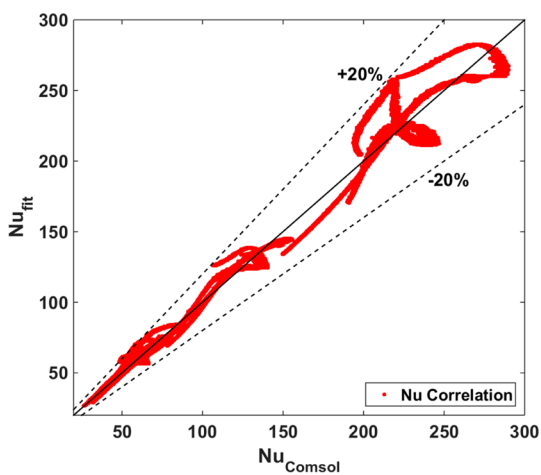

Figure 15. Nusselt correlations parity plot for SCW flow in a heated tube at low mass fluxes. Number of data points: 238 028.

considered in this work) on the radial temperature profile of the fluid. We can conclude that the reduction in the influence of buoyancy noticeable in the velocity profiles (decrease in the circulation zone with increasing mass flux

in Figure 10) is not substantial enough to affect the radial temperature profile and, by extension, the heat-transfer coefficient.

4.3. Effect of Tube Diameter. The influence of tube diameter on the flow profile is shown in Figure 13 for the conditions described in the figure caption (see Figure S7 for the axial mass flux plots). Increasing the tube diameter while maintaining the same mass flux leads to an increase in the sizes of the circulation and the stagnant zones, respectively. Figure 11 shows the variation of Gr/Re$^{2.7}$ over the tube length. An increase in the influence of buoyancy on the fluid flow is observed with an increase in the tube diameter.

The dimensionless radial temperature plot (Figure 14) shows a decrease in the dimensionless thermal boundary layer with an increase in tube diameter; however, the absolute thermal boundary layer thickness (taking the tube diameter into account) hardly changes.

4.4. Nusselt Correlation. Nusselt numbers calculated from the 2D COMSOL model are fitted to other dimensionless numbers (Gr, Re, and Pr) and fluid properties. The model parameters and dimensionless numbers that have been used for the data fitting are shown in Table 2.
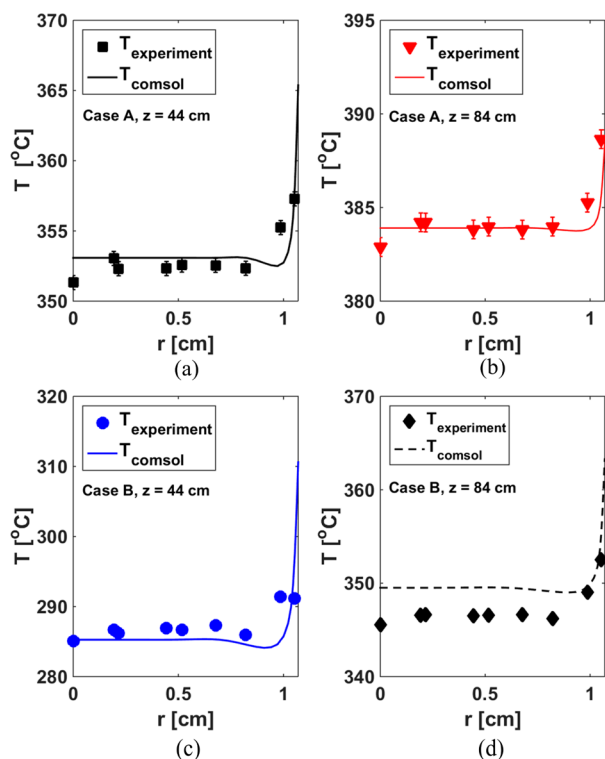
Figure 16. Comparison of radial temperature profiles obtained from 2D COMSOL simulation with experimental data for test cases A (a,b) and B (c,d).

We have fit our data to the correlation proposed by Mokry et al.:[9]

$$\text{Nu} = a \cdot \text{Gr}^{b} \cdot \text{Pr}^{c} \cdot \text{Rr}^{d} \cdot \left(\frac{\rho_w}{\rho_{mc}}\right)^{e} \cdot \left(\frac{C_{p,w}}{C_{p,mc}}\right)^{f} \cdot \left(\frac{\lambda_w}{\lambda_{mc}}\right)^{g} \cdot \left(\frac{\mu_w}{\mu_{mc}}\right)^{h}$$

(14)

which includes the effect of forced convection (Re), natural convection (Gr), and fluid properties (Pr), as well as a correction factor based on the difference in physical properties between the fluid in the bulk (mixing cup average) and the fluid at the wall. In eq 14, $a - h$ represent the fit parameters. The Nusselt fit obtained for the heated tube (Nu_t) is shown in eq 15.

The effect of diameter in Reynolds and Grashof has been taken into account in the Nusselt correlation for the heated tube by fitting to results obtained from simulations for 3 tube diameters (1, 2, and 4 cm, respectively) The Nusselt correlation fits within ±20% (Figure 15).

$$\text{Nu}_t = \frac{h_t d_t}{\lambda_{mc,t}} = 0.78 \cdot \text{Gr}^{0.34} \cdot \text{Re}^{-0.26}$$

$$\cdot \text{Pr}^{-0.07} \cdot \left(\frac{C_{p,w}}{C_{p,mc}}\right)^{0.20} \cdot \left(\frac{\rho_w}{\rho_{mc}}\right)^{0.23}$$

(15)

5. EXPERIMENTAL VALIDATION RESULTS

In this section, the validation of the 2D COMSOL model and the 1D Nusselt correlation for the test cases are discussed.

5.1. Validation of 2D COMSOL Model. The radial temperature profiles for cases A and B at tube length 44 and 84 cm are presented in Figure 16. The experimental results show a flat radial temperature profile in the fluid with a steep gradient at the near-wall region. The comparison of the numerical simulation results with the experimental data shows good agreement. This proves that the 2D COMSOL model correctly describes the radial temperature profiles for SCW flow at low mass fluxes.

5.2. Validation of 1D Nusselt Correlation and Predictive Accuracy of COMSOL. The derived 1D Nusselt correlation for the heated tube model has been validated. A 1D heated tube has been modeled with the test conditions listed in Table 3 as input parameters. In the 1D model, the heated tube is divided into sections. The steady-state heat balance for each section reads:

$$\dot{H}_{out} = \dot{H}_{in} + \dot{Q}_{wall}$$

(16)

The heat flow through the wall, $\dot{Q}_{wall}$, is calculated as

$$\dot{Q}_{wall} = U A_{sec}(T_{ow} - T_{mc})$$

(17)

where A_{sec} is the heat transfer area of each section, and U is the overall heat-transfer coefficient given as

$$\frac{1}{U} = \frac{d_t \ln(d_{ow}/d_{iw})}{2\lambda_w} + \frac{1}{h_t}$$
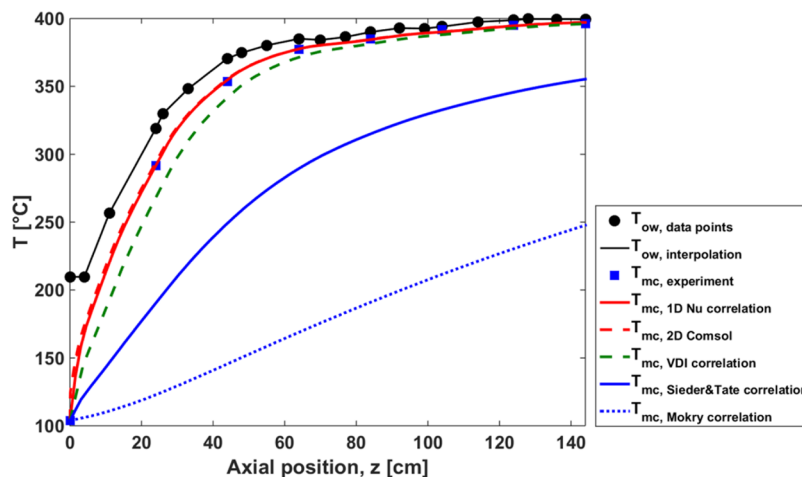
(18)

Figure 17. Experimental outer-wall and mixing-cup temperatures and mixing-cup temperature obtained from various Nusselt correlations for case A.
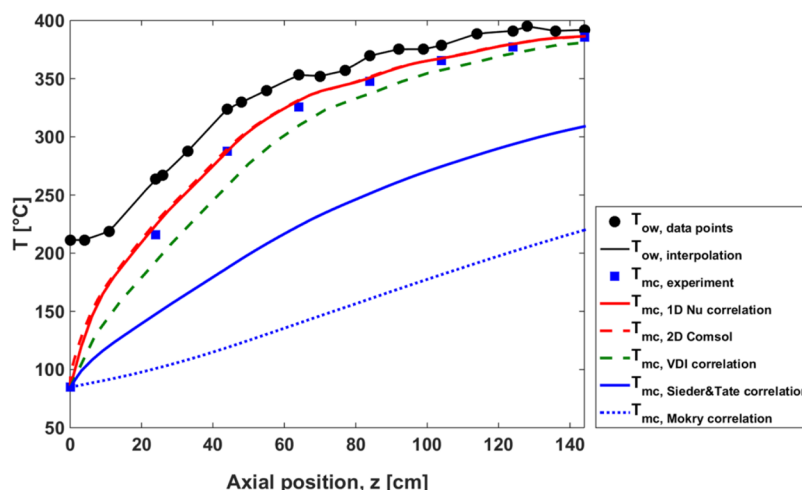
Figure 18. Experimental outer-wall and mixing-cup temperatures and mixing-cup temperature obtained from various Nusselt correlations for case B.

where d_{iw} is the inner tube diameter, d_{ow} is the outer tube diameter, and λ_w is the temperature-dependent thermal conductivity of the stainless steel wall.

The heat-transfer coefficient of the fluid in the tube (h_t) is obtained from the derived Nusselt correlation, eq 15. The 1D heated tube model was solved iteratively.

The results of the 1D validation for cases A and B are presented in Figures 17 and 18, respectively. In addition to the experimental results and the prediction from the proposed Nusselt correlation, predictions obtained using the VDI heat atlas[28] correlation (eq 19) for free convection, the Sieder–Tate[17] correlation (eq 21) for forced convection, the correlation of Mokry et al.[9] (eq 22) for turbulent supercritical water flow, and the results of 2D COMSOL simulations are also shown. The Sieder–Tate[17] correlation was chosen as it is one of the most widely used HTC for forced convection, while the VDI heat atlas[28] and Mokry et al.[9] HTC correlations were chosen because they are one of the most recent and experimentally validated correlations for the free convection and turbulent SCW flow, respectively.

$$Nu = \frac{h_t \cdot R}{\lambda} = 0.52 \cdot (Gr^* \cdot Pr)^{0.25} \qquad (19)$$

where Gr* is defined as

$$Gr^* = \frac{g \cdot \beta \cdot (T_{iw} - T_b) \cdot R^4 \cdot \rho^2}{\mu^2 \cdot L} \qquad (20)$$

The reference temperature for the properties is $\frac{1}{2}(T_{iw} - T_b)$.

$$Nu = \frac{h_t \cdot d_t}{\lambda} = 1.86 \cdot \left(Re \cdot Pr \cdot \frac{d_t}{L}\right)^{1/3} \cdot \left(\frac{\mu_b}{\mu_w}\right)^{0.14} \qquad (21)$$

$$Nu = \frac{h_t \cdot d_t}{\lambda} = 0.0061 \cdot \overline{Pr}_b^{0.684} \cdot Re_b^{0.904} \cdot \left(\frac{\rho_w}{\rho_b}\right)^{0.564} \qquad (22)$$

Results obtained with the Sieder–Tate and Mokry correlations significantly underestimate the experimental data. These correlations, derived for turbulent flows where forced convection is the governing mechanism for heat transport, are not suitable for low mass fluxes where natural convection governs the heat transport mechanism.

Although the VDI correlation performed much better than the forced convection correlations, it also under-predicts the measured temperature profiles. The VDI correlation has been derived for free convective flows under normal conditions of pressure and temperature and therefore cannot be applied to flows at sub- and supercritical conditions. However, we have shown that it is a good first estimate.

The comparison of the experimental data with the predicted mixing cup temperature obtained from the proposed Nusselt correlation and the results of the 2D COMSOL simulations show a good match.

6. CONCLUSIONS

A numerical study has been carried out in COMSOL Multi-physics CFD package to provide more insights into heat-transfer characteristics of supercritical water flow at low mass fluxes ($G \leq 20$ kg/m^2 s) in a heated tube. Using the SST turbulence model and including the volume force (to model natural convection) in the RANS equation are essential to accurately describe the flow. The 2D numerical results have been used to derive a 1D Nusselt correlation that can be used for quick engineering calculations. The numerical results and the proposed Nusselt correlation have been validated with experimental data.

An increased upward fluid velocity (about 10 times the inlet velocity) near the wall with a decreased velocity of the fluid in the bulk was observed. Buoyancy-induced circulation resulting from volume force (gravitational force) acting on density gradients (a direct consequence of temperature gradients) is created. Radial heat transport in the boundary layer is by conduction and convection, while away from the boundary layer, heat is primarily transferred by convection. The heat-transfer coefficient goes through a maximum as the temperature of the fluid approaches the pseudocritical temperature and then decreases rapidly at temperatures above the pseudocritical temperature.

It was shown that the influence of buoyancy decreases with increasing mass flux (for the same diameter, inlet conditions, and outer-wall temperature profile) and increases with increasing tube diameter (for the same mass flux, inlet conditions, and outer-wall temperature profile).

Radial fluid temperatures of SCW flow at low mass fluxes in a heated tube have been successfully measured in a newly

designed experimental apparatus at different axial positions. The numerical results are in good agreement with our experimental data. Temperature profiles obtained by using the proposed Nusselt correlation in a 1D heated tube model have been compared to our experimental data and widely used correlations for free and forced convection published in literature. The results of the proposed Nusselt correlation and the 2D COMSOL model for the heated tube show a good match with our experimental data.

■ ASSOCIATED CONTENT

Ⓢ Supporting Information
The Supporting Information is available free of charge on the ACS Publications website at DOI: 10.1021/acs.iecr.6b03268.

> Selected properties of water, the number of elements with corresponding grid sizes, mesh convergence for the 2D COMSOL SST, parameters for low-P–T turbulent water and turbulent SCW flow validation, Nu validation for flow under low P–T conditions, Nusselt validation of COMSOL, variation of axial mass flux along the tube radius at different axial positions, and variation of axial mass flux along the tube radius at different axial positions for different mass fluxes and tube diameters, respectively (PDF)

■ AUTHOR INFORMATION

Corresponding Author
*E-mail: a.g.j.vanderham@utwente.nl.

Notes
The authors declare no competing financial interest.

■ ACKNOWLEDGMENTS

■ NOMENCLATURE

A = heat-transfer area (m^2)
C_p = isobaric heat capacity (J/kg k)
CFD = computational fluid dynamics
d = diameter (m)
F = volume force $(kg/m^2 s^2)$
g = gravitational constant (m/s^2)
G = mass flux $(kg/m^2 s)$
Gr = Grashof number
h, HTC = heat-transfer coefficient $(W/m^2 \, °C$
H = enthalpy (J/kg)
$\dot{H}$ = rate of change of enthalpy (W)
$\mathbf{I}$ = identity tensor
k = turbulent kinetic energy (J/kg)
L = tube length (m)
Nu = Nusselt number
p = relative pressure (Pa)
P = absolute pressure (Pa)
Pr = Prandtl number
$\dot{Q}$ = heat flow (W)
r = radial coordinate (m)
R = tube radius (m)
Re = Reynolds number

SCW = supercritical water
SST = shear-stress transport
T = temperature (°C)
$\mathbf{u}$ = velocity vector (m/s)
U = overall heat-transfer coefficient $(W/m^2 \, K)$
y^+ = Near-wall grid resolution
z = axial coordinate (m)

Greek Symbols

β = thermal expansion coefficient (K^{-1})
ε = turbulent dissipation rate (m^2/s^3)
μ = dynamic viscosity (Pa s)
μ_T = turbulent viscosity (Pa s)
ρ = density (kg/m^3)
ϕ_h'' = heat flux (W/m^2)
ω = turbulence frequency (s^{-1})
λ = thermal conductivity (W/m K)

Subscripts

avg = average
b = bulk
c = critical
cond = conductive
conv = convective
eff = effective
in = inlet
iw = inner wall
mc = mixing cup average
ow = outer wall
pc = pseudocritical
sec = section
t = tube
T = turbulent
w = wall

■ REFERENCES

(1) Marcus, Y. *Supercritical water: A Green Solvent, Properties and Uses*; John Wiley & Sons: Hoboken, NJ, 2012.
(2) Kersten, S. R. A.; Potic, B.; Prins, W.; Van Swaaij, W. P. M. Gasification of Model Compounds and Wood in Hot Compressed Water. *Ind. Eng. Chem. Res.* **2006**, *45*, 4169−4177.
(3) Kruse, A. Hydrothermal biomass gasification. *J. Supercrit. Fluids* **2009**, *47*, 391−399.
(4) Schacht, C.; Zetzl, C.; Brunner, G. From plant materials to ethanol by means of supercritical fluid technology. *J. Supercrit. Fluids* **2008**, *46*, 299−321.
(5) Bermejo, M. D.; Cocero, M. J. Supercritical water oxidation: A technical review. *AIChE J.* **2006**, *52*, 3933−3951.
(6) Brunner, G. Near and supercritical water. Part II: Oxidative processes. *J. Supercrit. Fluids* **2009**, *47*, 382−390.
(7) Qian, L.; Wang, S.; Zhang, J. Experimental study on supercritical water oxidation of paper mill sludge. *Adv. Mater. Res. (Durnten-Zurich, Switz.)* **2014**, *955−959*, 711−715.
(8) Chen, Z.; Wang, G.; Yin, F.; Chen, H.; Xu, Y. A new system design for supercritical water oxidation. *Chem. Eng. J.* **2015**, *269*, 343−351.
(9) Mokry, S.; Pioro, I.; Farah, A.; King, K.; Gupta, S.; Peiman, W.; Kirillov, P. Development of supercritical water heat-transfer correlation for vertical bare tubes. *Nucl. Eng. Des.* **2011**, *241*, 1126−1136.
(10) Odu, S. O.; van der Ham, A. G. J.; Metz, S.; Kersten, S. R. A. Design of a Process for Supercritical Water Desalination with Zero Liquid Discharge. *Ind. Eng. Chem. Res.* **2015**, *54*, 5527−5535.
(11) Wagner, W.; Cooper, J. R.; Dittmann, A.; Kijima, J.; Kretzschmar, H. J.; Kruse, A.; Mares, R.; Oguchi, K.; Sato, H.; Stocker, I.; Sifner, O.; Takaishi, Y.; Tanishita, I.; Trubenbach, J.; Willkommen, T. The IAPWS industrial formulation 1997 for the

thermodynamic properties of water and steam. *J. Eng. Gas Turbines Power* **2000**, *122*, 150−182.

(12) Bishop, A. A.; Krambeck, F. J.; Sandberg, R. O. *High-temperature supercritical pressure water loop. III. Forced convection heat transfer to superheated steam at high pressure and high Prandtl numbers*; Westinghouse Elec. Corp.: Township, PA, 1964; p 101.

(13) Swenson, H. S.; Carver, J. R.; Kakarala, C. R. Heat transfer to supercritical water in smooth-bore tubes. *J. Heat Transfer* **1965**, *87*, 477−84.

(14) Yamagata, K.; Nishikawa, K.; Hasegawa, S.; Fujii, T.; Yoshida, S. Forced convective heat transfer to supercritical water flowing in tubes. *Int. J. Heat Mass Transfer* **1972**, *15*, 2575−93.

(15) Aicher, T.; Martin, H. New correlations for mixed turbulent natural and forced convection heat transfer in vertical tubes. *Int. J. Heat Mass Transfer* **1997**, *40*, 3617−3626.

(16) Withag, J. A. M.; Sallevelt, J. L. H. P.; Brilman, D. W. F.; Bramer, E. A.; Brem, G. Heat transfer characteristics of supercritical water in a tube: Application for 2D and an experimental validation. *J. Supercrit. Fluids* **2012**, *70*, 156−170.

(17) Bird, R. B.; Stewart, W. E.; Lightfoot, E. N. *Transport Phenomena*, revised 2nd ed.; John Wiley & Sons, Inc.: New York, 2007.

(18) Versteeg, H. K.; Malalasekera, W. *An Introduction to Computational Fluid Dynamics - The Finite Vol. Method*, 2nd ed.; Pearson Education Limited: London, 2007.

(19) Metais, B.; Eckert, E. R. G. Forced, Mixed, and Free Convection Regimes. *J. Heat Transfer* **1964**, *86*, 295−296.

(20) Menter, F. R.; Kuntz, M.; Langtry, R. Ten Years of Industrial Experience with the SST Turbulence Model. In *Turbulence and Heat Mass Transfer*; Hanjalic, K.; Nagano, Y.; Tummers, M., Eds.; Begell House, Inc.: New York, NY, 2003; pp 625−632.

(21) Comsol. *CFD Module User's Guide*; COMSOL: Burlington, MA, 2014; pp 171−174.

(22) Kays, W. M.; Crawford, M. E.; Weigand, B. *Convective Heat and Mass Transfer*; 4th ed.; McGraw-Hill: Singapore, 2005.

(23) Tritton, D. J. *Physical Fluid Dynamics*; 2nd ed.; Clarendon Press: Oxford, U.K., 1988.

(24) Huber, M. L.; Perkins, R. A.; Friend, D. G.; Sengers, J. V.; Assael, M. J.; Metaxa, I. N.; Miyagawa, K.; Hellmann, R.; Vogel, E. New International Formulation for the Thermal Conductivity of H_2O. *J. Phys. Chem. Ref. Data* **2012**, *41*, 0331021−03310223.

(25) Huber, M. L.; Perkins, R. A.; Laesecke, A.; Friend, D. G.; Sengers, J. V.; Assael, M. J.; Metaxa, I. N.; Vogel, E.; Mareš, R.; Miyagawa, K. New International Formulation for the Viscosity of H_2O. *J. Phys. Chem. Ref. Data* **2009**, *38*, 101−125.

(26) Holmgren, M. *XSteam for MATLAB*, 2006.

(27) Jackson, J.; Hall, W. Influences of buoyancy on heat transfer to fluids flowing in vertical tubes under turbulent conditions. In *Turbulent Forced Convection in Channels and Bundles*; McGraw-Hill: New York, 1979; Vol. 2, pp 613−640.

(28) Kast, W.; Klan, H. Heat Transfer by Free Convection: Special Cases. In *VDI Heat Atlas*, 2nd ed.; Springer-Verlag Berlin Heidelberg: Heidelberg, Germany, 2010; pp 681−684.